AGU PUBLICATIONS

JGR

Journal of Geophysical Research: Earth Surface

RESEARCH ARTICLE
10.1002/2015JF003549

Key Points:
- Classification of bed form interactions during dune pattern coarsening
- Effect of the depth and strength of the flow on the giant dune fields
- Superimposed bed forms and sedimentary patterns in giant dune fields

Correspondence to:
X. Gao,
gao@ipgp.fr

Citation:
Gao, X., C. Narteau, and O. Rozier (2015), Development and steady states of transverse dunes: A numerical analysis of dune pattern coarsening and giant dunes, *J. Geophys. Res. Earth Surf.*, *120*, 2200–2219, doi:10.1002/2015JF003549.

Received 16 MAR 2015
Accepted 21 SEP 2015
Accepted article online 24 SEP 2015
Published online 29 OCT 2015

Development and steady states of transverse dunes: A numerical analysis of dune pattern coarsening and giant dunes

Xin Gao[1], Clément Narteau[1], and Olivier Rozier[1]

[1] Institut de Physique du Globe de Paris, Sorbonne Paris Cité, Université Paris Diderot, UMR 7154 CNRS, Paris, France

Abstract We investigate the development and steady states of transverse dunes for ranges of flow depths and velocities using a cellular automaton dune model. Subsequent to the initial bed instability, dune pattern coarsening is driven by bed form interactions. Collisions lead to two types of coalescence associated with upstream or downstream dominant dunes. In addition, a single collision-ejection mechanism enhances the exchange of mass between two adjacent bed forms (throughpassing dunes). The power law increases in wavelength and amplitude exhibit the same exponents, which are independent of flow properties. Contrary to the wavelength, dune height is limited not only by flow depth but also by the strength of the flow. Superimposed bed forms may propagate and continuously destabilize the largest dunes. We identify three classes of steady state transverse dune fields according to the periodicity in crest-to-crest spacing and the mechanism of size limitation. In all cases, the steady state is reached and maintained through the dynamic equilibrium between flow strength and dune aspect ratio. In the limit of low flow strength, where it becomes the primary factor of size limitation, the bed shear stress in the dune trough regions is close to its critical value for motion inception. Comparisons with natural dune fields suggest that many of them may have reached a steady state. Finally, we infer that the sedimentary patterns in the model may be used to bring new constraints on the development of modern and ancient dune fields.

1. Introduction

Transverse dunes form under quasi-unidirectional flows in regions of abundant sand supply [*Wasson and Hyde*, 1983; *Courrech du Pont et al.*, 2014]. They have an asymmetrical shape with an upstream slope of approximately 10°, a slip face in the lee, and smooth ridges perpendicular to the resultant sand flux. In the vast majority of cases, transverse dune fields exhibit both a clear periodicity at large length scale and a wide variety of smaller superimposed bed forms on the stoss slopes of larger dunes (Figure 1). This apparent complexity may reflect fluctuations in flow speed and direction, variations in grain size distribution, and changes in sand availability (e.g., barchanoid ridges) or in subsurface properties (e.g., water table depth) [*Kocurek and Ewing*, 2005; *Best*, 2005; *Ewing et al.*, 2006]. Nevertheless, it may also result purely from the internal dynamics of a population of transverse dunes during the formation and evolution of dune fields [*Elbelrhiti*, 2005; *Jerolmack and Mohrig*, 2005; *Kocurek and Ewing*, 2005]. More than the changes in the physical environment, it is then critical to focus on dune pattern coarsening as well as on the formation and growth of secondary bed forms [*Zhang et al.*, 2010].

Starting from a flat sand bed, the preliminary stage for the formation of dunes is now firmly grounded in a theoretical framework supported by a growing body of field and experimental evidences [see *Courrech du Pont*, 2015, and references within]. All together, they clearly establish that the initial phase, also called the dune instability, is dominated by the emergence of a regular undulation with a constant wavelength (e.g., $\approx$ 20 m for aeolian dunes on Earth) and an exponentially growing amplitude [*Kroy et al.*, 2002a; *Hersen et al.*, 2002; *Elbelrhiti et al.*, 2005; *Claudin and Andreotti*, 2006]. Subsequent to this linear regime, the formation of transverse dune fields relies on nonlinear pattern coarsening as a result of dune-dune interaction, amalgamation or nucleation of secondary bed forms [*Coleman and Melville*, 1994; *Coleman et al.*, 1996; *Kocurek et al.*, 2010]. Given the complex nature of this gradual increase in dune size and wavelength, current research has only focused on the conditions under which such a coarsening occurs or on the factors that can interrupt this process when a characteristic length scale is selected, for example according to the aerodynamic roughness length [*Pelletier*, 2009] or flow depth [*Politi and Misbah*, 2004; *Valance*, 2011].

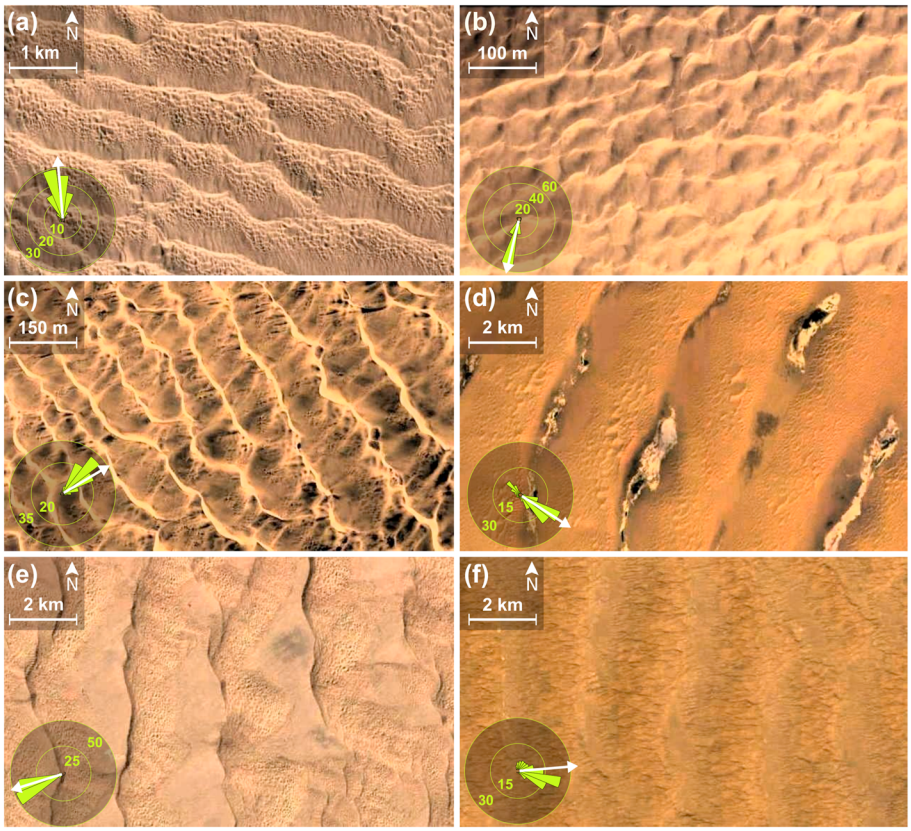

Figure 1. Transverse dune fields in arid deserts on Earth: (a) The Namib Sand Sea (Namibia, 26°09′S, 15°05′E, RDP/DP = 0.87). (b) The Atlantic Sahara desert (Morocco, 28°02′N, 12°12′E, RDP/DP = 0.85). (c) The Moçâmedes desert (Angola, 16°32′S, 12°00′E, RDP/DP = 0.88). (d) The East Badain Jaran desert (China, 38°38′N, 105°04′E, RDP/DP = 0.40). (e) The East Taklamakan desert (China, 39°27′N, 87°20′E, RDP/DP = 0.82). (f) The Registan desert (Afghanistan, 30°41′N, 65°40′E, RDP/DP = 0.76). See Appendix B for the estimation of the RDP/DP values from wind data. The white arrow indicates the resultant drift direction.

The dependence of dune height on flow depth has been the subject of considerable attention in fluvial research [*Allen*, 1963; *Yalin*, 1964; *Jackson*, 1976; *Richards*, 1980]. Although the role of the free surface of water is critical for the development of other bed forms (e.g., antidunes and upstream propagating bed forms), the initiation of dunes can be explained without the need to invoke a fluid density boundary. Basically, as soon as the streamlines are compressed upstream of their crests and diverge downstream, dunes can develop equally well in closed conduits or assuming an infinite flow depth. In the limit of high flow depth, the near-surface flow over a topographic undulation is perturbed to a distance which is proportional to the characteristic wavelength of the bed elevation profile. In this case, thanks to its inertia, the upper fluid region serves as a confinement layer. On the opposite, if the flow depth is smaller than the characteristic wavelength of the bed elevation profile, the flow perturbation occurs now on a characteristic height which is set by flow depth. As this flow depth is decreasing, flow velocity and sediment transport rapidly increase at the top of the dunes, so that they cannot continue to grow in height. This is true whatever the top boundary condition (i.e., a free surface or a rigid wall [see *Charru et al.*, 2013, and references therein]).

The presence of a free surface has been recognized to have a feedback on subaqueous dune morphology, especially on dune height which has been shown to scale from one half to one sixth of flow depth [*Yalin*, 1977; *Allen*, 1985; *Flemming*, 2000; *Unsworth et al.*, 2013]. Following *Andreotti et al.* [2009], similar behaviors may be observed in aeolian systems due to the presence of the atmospheric boundary layer (ABL), the lowest part of the atmosphere in which radiative forcing causes turbulent vertical mixing. As a result, both horizontal wind velocity and temperature may be homogeneous until an altitude F, which determines the depth of the flow. Above, the linear stratification of the air density profile is responsible for a free-stream flow. This inversion layer stands as a top boundary condition that confines the flow in the ABL. A few unresolved problems remain with this aeolian analogy to the water depth in subaqueous systems. First, the boundary between the ABL and the

free-stream flow has to be considered as immiscible, as water in the air. Second, the depth of the ABL varies broadly over different timescales due to its strong dependence on temperature [*Stull*, 1988]. Then, it is quite difficult to define the height of a capping layer with precision, and the overall effect of confinement may be more complicated to investigate. However, the empirical data shown by *Andreotti et al.* [2009] reveal a clear linear relationship between the depth of the ABL and the characteristic wavelength of transverse bed forms. Then, similarities in the flow depth saturation mechanism in both subaqueous and aeolian systems deserve to be investigated. Within this context, we do not test the existence of a capping layer. Instead, we design numerical experiments to analyze the effect of a perfectly flat and undisturbed top boundary condition on the development and steady state of a granular bed sheared by an unidirectional flow.

Andreotti et al. [2009] define giant dunes as bed forms that exhibit a characteristic wavelength proportional to flow depth (e.g., water depth for subaqueous dunes and the depth of the ABL for aeolian dunes). Starting from a small perturbation of a flat sand bed, their stability analysis also suggests that there is a wide range of unstable wavelengths that may enhance coarsening following the initial generation of dunes. Ultimately, as the amplitude of the bed forms is increasing, the confinement of the flow inhibits dune growth. Then, dune fields may reach a steady state by selecting a characteristic wavelength associated with their giant size. However, many questions remain on the morphodynamics of transverse dunes as they approach such a steady state, especially in the presence of superimposed bed forms.

Bed forms in unidirectional flow have now been examined though different types of subaqueous laboratory experiments [*Southard*, 1991; *Coleman and Melville*, 1994; *Bennett and Best*, 1995; *Coleman and Melville*, 1996; *Coleman et al.*, 1996; *Raudkivi*, 1997; *Venditti et al.*, 2005; *Reffet et al.*, 2010]. Nevertheless, despite all these efforts, there is still no comprehensive theory to explain the diversity of observed shapes and sizes during the development of dunes [*Best*, 2005; *Jerolmack and Mohrig*, 2005]. Not surprisingly, this is even more the case for natural subaqueous and aeolian dune fields, where initial and boundary conditions remain unknown. As a consequence, the evolution and the steady state of transverse dune fields are usually inferred from indirect evidence such as the density of defects [*Werner and Kocurek*, 1999] or the cumulative probability of dune height and spacing measurements [*Ewing et al.*, 2006; *Dong et al.*, 2009]. Furthermore, dynamical dune features cannot be directly reproduced in wind tunnel experiments because of the existence of a minimum dune size [*Hersen et al.*, 2002]. Instead, many of these experiments have concentrated on air flow properties above a predefined topography to estimate the distribution of the basal shear stress [*Parsons et al.*, 2004; *Walker and Nickling*, 2003; *Dong et al.*, 2007; *Qian et al.*, 2009]. Coupled with the available set of data on natural dune fields [*Wiggs et al.*, 1996; *Parteli et al.*, 2006; *Baddock et al.*, 2007], they suggest that in addition to the crestal area, the interdune dynamics may significantly contribute to the morphology of the sand dune system.

Here we numerically investigate the nonlinear evolution of bed forms that develop after the initial bed instability. Our objective is to characterize dune pattern coarsening and the steady states of transverse dune fields with respect to two control parameters, the depth and the strength of the flow. With this goal in mind, we use a real-space cellular automaton dune model that offers three major advantages over traditional numerical methods. First, it has a confined flow, which continuously adapts according to the topography. Thus, it advances the current set of cellular automaton approaches [*Nishimori and Ouchi*, 1993; *Werner*, 1995; *Nishimori et al.*, 1998; *Momiji et al.*, 2000], allowing for the modeling of the feedback of a top boundary condition on a growing topography. Second, it is based on a fully coupled system between fluid and granular phases, which has shown to produce a wide range of emergent dune features such as superimposed bed forms [*Narteau et al.*, 2009] or arm growth [*Zhang et al.*, 2012]. Then, this numerical approach can address both the development of dunes and the role of secondary bed forms without assigning predefined relationships between recirculation flows, topography, and basal shear stress, as is usually done in continuous [*Sauermann et al.*, 2001; *Kroy et al.*, 2002b; *Andreotti et al.*, 2002; *Schwämmle and Herrmann*, 2004; *Fischer et al.*, 2008] or more realistic discrete dune models [*Pelletier*, 2009]. Third, the three-dimensional cellular space can be used for the tracking of individual particles and the mapping of sedimentary structures. Hence, in addition to the morphodynamics features, it is possible to bring new insights into the migration history of sediment particles [*Zhang et al.*, 2014] and into changes in stratification patterns [*Zhang et al.*, 2012]. This is particularly important to distinguish interaction bounding surfaces from other types of sedimentary structures [*Brookfield*, 1977].

This paper is organized as follows. After a brief presentation of the real-space cellular automaton dune model in section 2, numerical results are used to describe the joint evolution of basal shear stress and topography during the coarsening phase (section 3). Then, we discuss the influence of both flow depth and strength on the

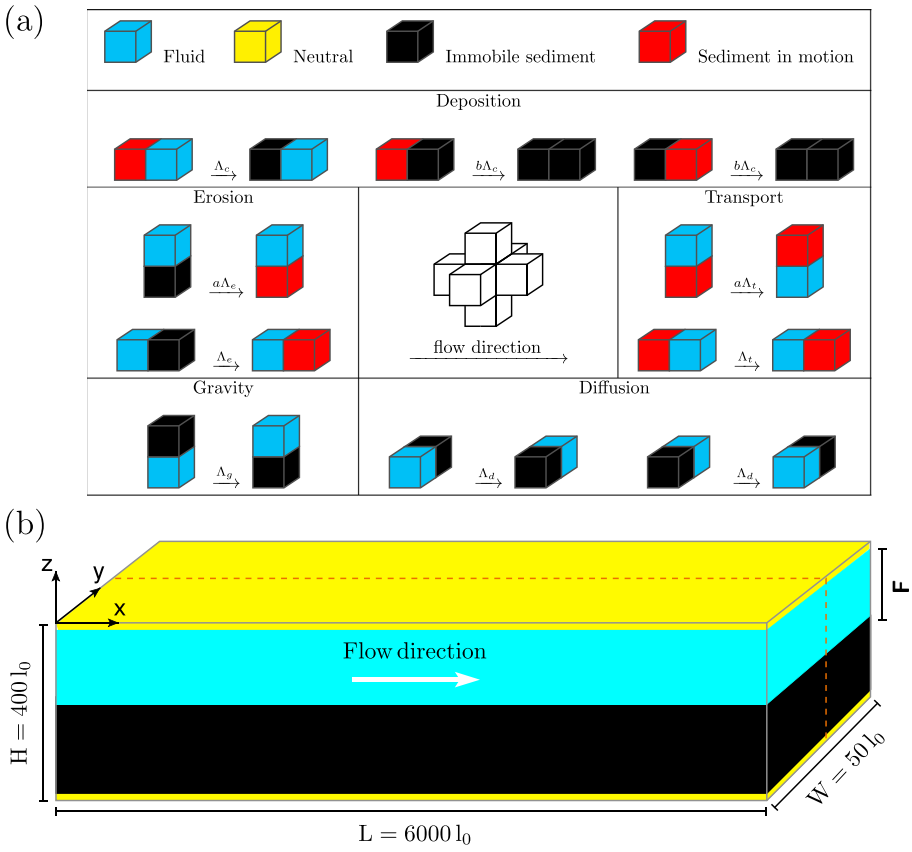

Figure 2. The cellular automaton dune model. (a) Active transitions of doublets in the model of sediment transport. Different sets of transition are associated with deposition, erosion, transport, and diffusion. $\{\Lambda_c,\ \Lambda_e,\ \Lambda_t,\ \Lambda_g,\ \Lambda_d\}$ are transition rates in units of t_0^{-1}. They are constant except for Λ_e that depends on the basal shear stress according to equation (2). *a* and *b* are positive constants. The central inset shows the direction of the unidirectional flow and the orientation of the nearest neighbors in a regular cubic lattice. Neutral cells are used to shape the virtual environment. (b) Initial condition in the cellular space. Note the finite flow depth *F* and the thick sediment layer that ensure that the dunes will never reach the nonerodible ground (i.e., no change in sand availability).

long-term behavior of transverse dune fields (section 4). Keeping in mind that all these numerical results may also be used to interpret behaviors of sediment bed forms in subaqueous environments and other planetary bodies, we conclude by comparing the predictions of the numerical model with observations in terrestrial aeolian sand seas (section 5).

2. A Real-Space Cellular Automaton Dune Model

The real-space cellular automaton dune model combines a traditional cellular automaton of sediment transport with a lattice gas method for the simulation of a turbulent flow over an erodible bed (see *Chopard and Droz*, 1998 [1998] for a review). In this model presented in full detail in *Narteau et al.* [2009], the physical environment is fully described by a 3-D lattice of cells with a finite number of states (Figure 2a). Then, the dynamical system is entirely based on next-neighbor interactions at the elementary length scale l_0 of the cubic lattice [*Narteau et al.*, 2001; *Rozier and Narteau*, 2014].

The model of sediment transport is governed by sets of transitions within pairs of nearest-neighbor cells, the so-called doublets. Each set of transitions is associated with an individual physical process (e.g., erosion, deposition, and transport) and a characteristic timescale expressed in units of t_0 (Figure 2a). All transitions are incorporated into a continuous time stochastic process to produce a global dynamical system devoted to the formation and evolution of bed forms. In addition, to take into account avalanching, we impose an angle of repose for the granular material [*Zhang et al.*, 2014].

To simulate fluid flow, we implement a lattice gas cellular automaton that converts discrete motions of a finite number of fluid particles into physically meaningful quantities. To reduce the computation time, we do not consider a 3-D flow and there is no transverse secondary flow in the model. Instead, we consider a set of uniformly spaced vertical planes parallel to the direction of the flow. Fluid particles are confined to these 2-D planes and they can fly from cell to cell along the direction specified by their velocity vectors. Then, their collision dynamics impose fluxes of particles that can be converted into a fluid velocity field $\vec{V}$ by averaging over space and time at the elementary length scale l_0 of the model of sediment transport.

At the bottom of the cellular space, we consider a no-slip boundary condition: all fluid particles that collide with sedimentary cells bounce back along their incident direction. Thus, the velocity field is null at the sediment-fluid interface, and there is a permanent feedback of the topography on the fluid flow. As a result, this model spontaneously produces flow recirculation on the lee side of dunes and an increase in flow velocity on their stoss side [see *Narteau et al.*, 2009, Figures 4 and C1]. It also generates a logarithmic vertical velocity profile from which it is possible to derive the shear velocity (see equation (1)) as well as an aerodynamic roughness length. Not surprisingly, this characteristic length is given by the elementary length scale l_0 of our cellular space. As this length scale is a few orders of magnitude larger than grain size in nature, it is impossible to directly test any hypothesis regarding how dune properties might relate to the aerodynamic roughness length.

The flow continuously modifies the topography through sediment transport in zones where the basal shear stress is high enough to mobilize sedimentary particles. In practice, we estimate the effect of flow velocity on the erosion rate Λ_e (Figure 2a). The basal shear stress is defined as

$$\tau_s = \tau_0 \frac{\partial \vec{V}}{\partial \vec{n}}, \tag{1}$$

where $\vec{n}$ is the normal to the topography and τ_0 is the stress scale of the model. Then, we consider that the erosion rate Λ_e is linearly related to the bed shear stress τ_s according to

$$\Lambda_e(\tau_s) = \begin{cases} 0 & \text{for } \tau_s \leq \tau_1, \\ \Lambda_0 \dfrac{\tau_s - \tau_1}{\tau_2 - \tau_1} & \text{for } \tau_1 \leq \tau_s \leq \tau_2, \\ \Lambda_0 & \text{else}, \end{cases} \tag{2}$$

where Λ_0 is a constant rate, τ_1 is the threshold for motion inception and τ_2 is a parameter to adjust the slope of the linear relationship. For consistency, we always have $\tau_2 \gg \tau_s$. By definition, $(\tau_s - \tau_1)$ is the excess shear stress from which we can derive flow strength. Hence, we can use the threshold shear stress to modify the strength of the flow in the model: the higher the τ_1 value is, the smaller the strength of the flow [see, *Narteau et al.*, 2009, Figure 7].

At the top of cellular space, the flow is confined by a flat layer of neutral cells (Figure 2b). Along this layer, we consider a free-slip boundary condition: all fluid particles that collide with this surface change only the sign of the vertical component of their velocity vectors. Thus, the horizontal component of the flow is conserved, and the geometrical confinement of the flow may lead to the compression of streamlines over the entire flow depth when the wavelength of the bed elevation profile and flow depth are on the same order of magnitude (see section 1).

In this cellular automaton dune model, the elementary time and length scales $\{l_0, t_0\}$ are entirely defined with respect to the bed instability mechanism using the most unstable wavelength and the averaged saturated sand flux [*Narteau et al.*, 2009]. As shown in Table 2 of *Zhang et al.* [2014], the model can then be used in all types of physical environments where the dune instability is observed to provide quantitative estimates of the evolution of dune fields. From a more theoretical point of view, this rescaling strategy also permits the model to overcome the fundamental limitation related to the arbitrariness of the choice of the elementary length scale inherent to a cellular automaton approach.

Figure 2b shows the initial condition for all simulations. It can be described as an elongated rectangular flume of length $L = 6000\, l_0$, width $W = 50\, l_0$, and height $H = 400\, l_0$, covered by a thick layer of sedimentary cells. We use periodic boundary conditions in horizontal directions. However, the relatively small width of the cellular space limits the development of three-dimensional bed forms to concentrate only on the longitudinal

interaction between adjacent dune patterns. More exactly, we investigate the influence of flow velocity using five threshold shear stress values $\tau_1/\tau_0 = \{0, 5, 10, 15, 20\}$. For each of them, we also examine the influence of flow depth, $F/l_0 = \{60, 80, 100, 120, 140, 160\}$, by changing the thickness of the sedimentary layer. Note that in all cases $H/F > 2.5$, such that it is impossible for bed forms to reach the layer of neutral cells that forms the nonerodible basement at the bottom of the cellular space (i.e., no change in sediment availability). All these boundary and initial conditions ensure that dune patterns can evolve to steady states that do not depend on sediment supply, another free parameter which could be independently explored [*Eastwood et al.*, 2011].

At any given time step in the model, we can save the topography built by the immobile sedimentary cells, the flow field, and the state of the 3-D cellular space (i.e., state of all cells, position and orientation of the velocity vector of fluid particles). In addition, we can record all the transitions of doublet and the corresponding physical mechanism (see Figure 1a) to track sedimentary cells or locally estimate sand flux [*Zhang et al.*, 2014]. All these sources of information are used to quantify dune morphodynamics in the model.

3. Development of Transverse Dunes

In their seminal paper, *Coleman and Melville* [1994] describe the evolution of subaqueous bed features following their initial generation from a flat sand bed in a 12 m long flume. Here we follow the same presentation to facilitate the comparison of these experimental results with our numerical data.

3.1. General Bed Form Development

Figure 3 shows space-time diagrams of the long-term development of bed forms for the same flow strength but for two different flow depths. As the coarsening proceeds, the observed increase in contrast intensity reflects the dune growth rate. Simultaneously, dune speed is decreasing and the slopes of the diagonal stripe patterns increase. For shallow flow depth, bed forms rapidly reach a regular steady state with a well-established amplitude and wavelength (Figures 3a and 3f).

For larger flow depth, the elevation profile is constantly changing through dune-dune interactions and the formation of secondary bed forms on the stoss slopes of larger dunes (Figure 3b). These dynamical features sustain the structural complexity of the dune field to finally give rise to an irregular steady state (Figures 3c–3e). Except by chance, there is no selection of a dominant wavelength. Instead, there is a wide range of bed forms spanning at least 2 orders of magnitude in wavelength (Figure 3g). If this observed range of spectral properties is maintained by the systematic development of new generations of superimposed dunes (Figure 3d), there is also an upper limit in dune size indicating the end of the growth phase (see section 4).

During the coarsening process, Figure 4 shows that both the amplitude and wavelength exhibit a power law behavior with the same exponent of 1/3 [*Werner and Kocurek*, 1999]. As this behavior is observed within the ranges of parameter values studied, it seems to be controlled more by collision dynamics (i.e., dune-dune interactions) rather than flow depth and strength. Nevertheless, flow depth and strength influence the steady state of bed forms leading to different upper limits in dune height and spacing.

3.2. Mechanics of Bed Form Development

Dune pattern coarsening mainly results from dune collisions induced by heterogeneities in bed form migration rates. Individual dunes propagate with a speed which is inversely proportional to their height [*Bagnold*, 1941]. Smaller ones run into and coalesce with larger ones to increase their size. However, the dune velocity is also directly proportional to the sand flux at the crest, which is a function of the speedup of the flow over the local topography [*Jackson and Hunt*, 1975]. As a result, *Zhang et al.* [2010] have shown that there is not an universal dune shape and that the dune aspect ratio may significantly change according to flow properties (e.g., flow strength and top boundary conditions). In this case, the only way to compare the morphodynamics of a population of dunes is to normalize their speed by the overall sand flux at their crest [see *Zhang et al.*, 2010, Figure 9]. Here we first check that all the primary and secondary dunes produced by the model respect the same relationship. Then, putting aside the evaluation of dune speed, we focus on the various types of interacting dune features that control the development of bed forms and their increase in size.

In order to locate local maxima and minima in a digital elevation map or in a space-time diagram, we calculate the divergence of the normalized gradient

$$M = \mathrm{div}\left(\frac{\nabla h}{\|\nabla h\|}\right). \tag{3}$$

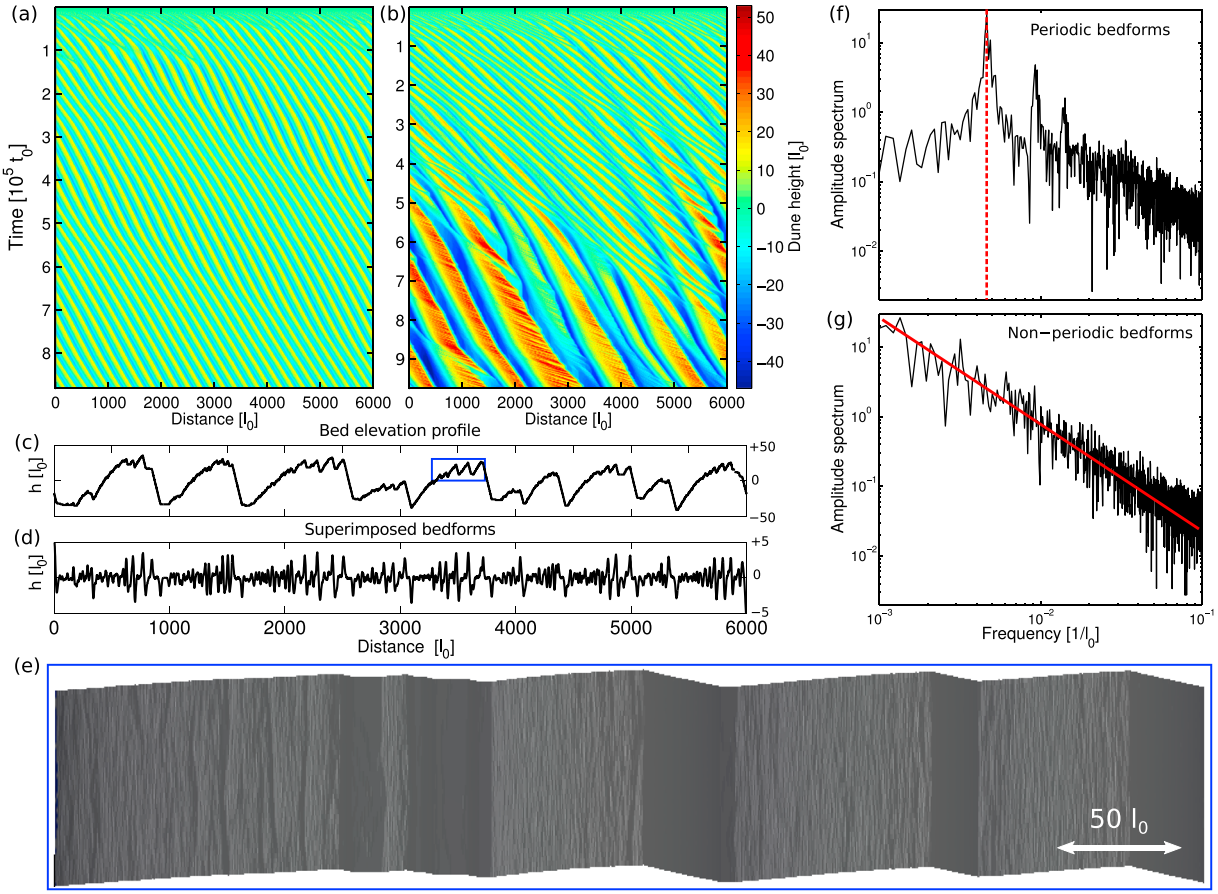

Figure 3. Development of dune patterns. Space-time diagrams of the topography measured along a vertical cross section parallel to the flow for $\tau_1/\tau_0 = 10$ and two different flow depths: (a) $F/l_0 = 80$ and (b) $F/l_0 = 160$. The dune height is the difference between the local elevation and the initial elevation of the flat bed. Note the presence of faster superimposed dunes on the stoss slope of larger dunes in Figure 3b. (c) Two-dimensional dune elevation profile at $t/t_0 = 8.3 \times 10^5$ for $F/l_0 = 160$ (Figure 3b). (d) Residual topography obtained by removal of the mean elevation averaged over a distance of $40\,l_0$ (i.e., the most unstable wavelength for the formation of dunes). (e) Three-dimensional dune elevation profile in the blue box of Figure 3c. (f) Fast Fourier transform of the 2-D dune elevation profile at $t/t_0 = 8.5 \times 10^5$ for $F/l_0 = 80$ (Figure 3a). The vertical dashed line corresponds to the characteristic wavelength of 214 l_0 of the periodic bed forms. Due to the triangular shape of the train of transverse dunes, secondary peaks are odd harmonics of the characteristic wavelength. (g) Fast Fourier transform of the 2-D dune elevation profile shown in Figure 3c. There is no characteristic wavelength, and the red line has a slope of $-3/2$.

Figure 5a shows the M map for the highest flow depth ($F/l_0 = 160$) and maximum flow strength ($\tau_1/\tau_0 = 0$) among all the simulations. The color map is saturated to enhance the contrast and track the position of dune crests (blue) and troughs (red). This representation allows to visualize collision dynamics from space-time diagram trajectories (Figures 5b–5d). Despite the apparent complexity of bed forms, three major types of interacting features are recognized [*Endo et al.*, 2005; *Vermeesch*, 2011; *Hugenholtz and Barchyn*, 2012].

1. *Collision and coalescence into a downstream dominant bed form*. A dune collides and merges into a bigger one downstream. As the upstream dune propagates, it may decrease in size and deposits its sediment on the stoss side of the impacted dune. This is enhanced by the steepness of the longitudinal and transverse slopes of the impacted dunes and by changes in bed shear stress on the secondary bed forms. Finally, the smaller dune disappears and the dominant downstream bed feature has increased in size. As it proceeds, the impacting dune accelerates, its slip face disappears and, downstream, the next discontinuity in topography is a crest that slows down (Figure 5b).
2. *Collision and coalescence into an upstream dominant bed form*. A smaller dune collides and grows at the expense of the dune on which it propagates. As the upstream impacting dune approaches the summit, it becomes higher than the impacted dune, which in turn propagates more rapidly. Then, both dunes start to separate again. However, the downstream dune is now in the recirculation zone of the dominant upstream bed feature. The magnitude of the basal shear stress on its stoss slope is significantly smaller than when

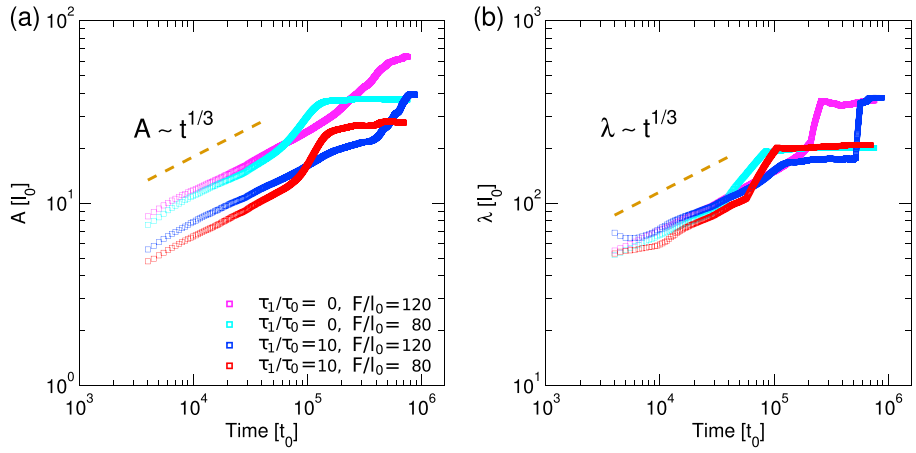

Figure 4. Evolution of the (a) amplitude and (b) wavelength of the bed elevation profile with respect to time. The autocorrelation function, $C(\lambda, l, t) = \langle h(\lambda, x, t)h(\lambda, x + l, t)\rangle - \langle h(\lambda, x, t)\rangle^2$, gives the amplitude $A(\lambda, t) = 2\sqrt{2C(\lambda, 0, t)}$ and the wavelength (the position of the first peak). In both cases, the dashed line corresponds to a power law increase with an exponent of 1/3. Due to the finite length of the cellular space, an error in wavelength of $\pm 25\ l_0$ should be considered for the largest dunes over long times.

it was directly exposed to the flow. Consequently, the downstream dune flattens. All the sediment that reaches its crest is trapped in an avalanche face, which has become abnormally high in comparison with an upstream stoss slope that continues to propagate. As a result, the impacted dune progressively disappears within its own slip face, which ultimately merges with the avalanche face of the decelerating impacting dune (Figure 5c).

3. *Collision and ejection with no dominant bed form*. A dune collides and exchanges mass with a bigger one downstream, which eventually becomes smaller and detaches. This mass exchange mechanism is repeated downstream, and the corresponding defects propagate at the speed of the ejected dunes. It gives rise to a

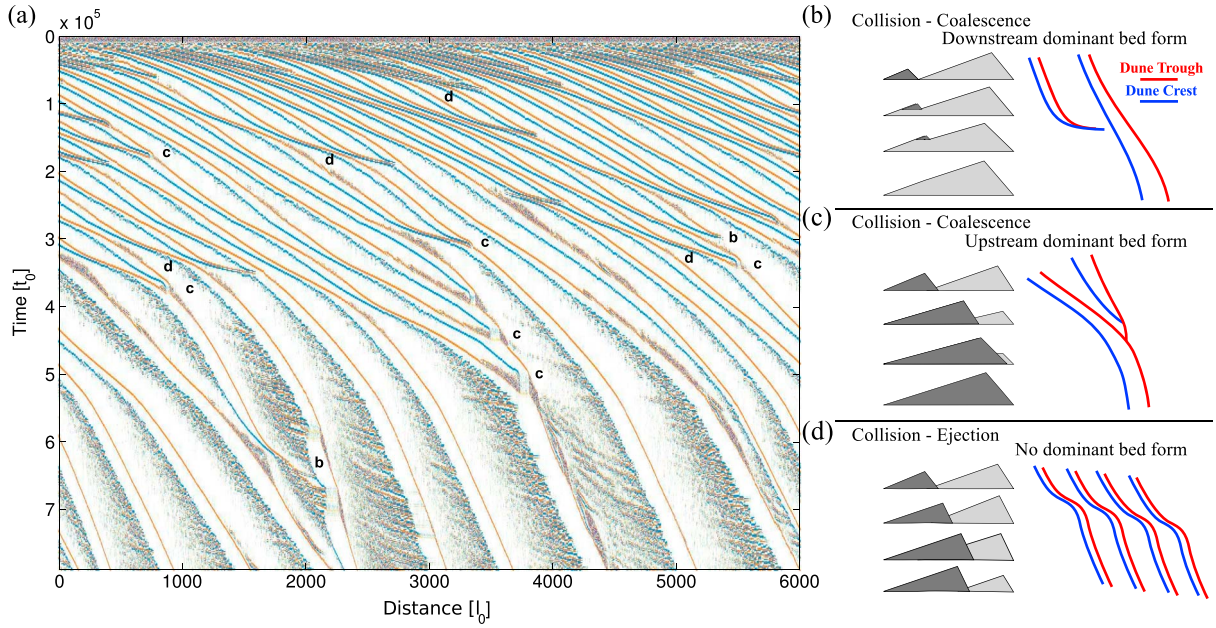

Figure 5. Classification of dune interactions during the coarsening phase. (a) Space-time diagram of crests (blue) and valleys (red) for $\tau_1/\tau_0 = 0$ and $F/l_0 = 160$ (the *M* map; see equation (3)). Note the development of superimposed bed forms on the stoss slope of larger dunes for $t/t_0 > 3 \times 10^5$. Schematic diagrams for three types of dune-dune interaction: (b) collision and coalescence into a downstream dominant bed form, (c) collision and coalescence into an upstream dominant bed form, and (d) collision and ejection with no dominant bed form (i.e., throughpassing dunes). The upstream and downstream dunes are shown in dark and light gray, respectively. Blue and red lines show the corresponding dynamics of crests and valleys, respectively. Different types of interacting features are marked in Figure 5a with the corresponding letters.

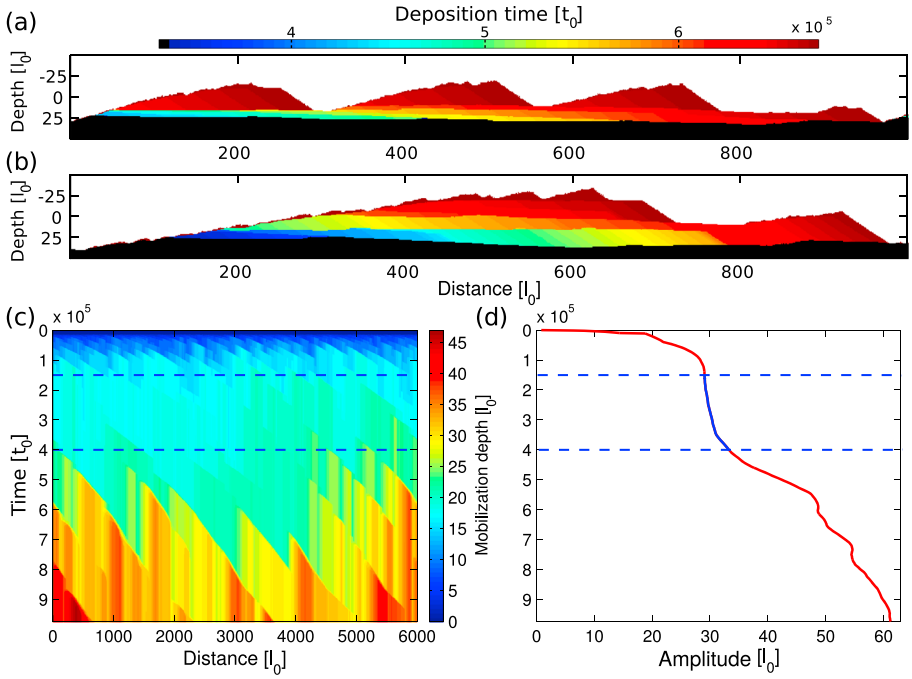

Figure 6. Sedimentary structures and mobilization depth during the development of bed forms. (a, b) Deposition time of sedimentary cells along vertical cross sections parallel to the flow direction for $\tau_1/\tau_0 = 10$, $F/l_0 = 60$ at $t/t_0 = 6.4 \times 10^5$. Black cells have never been mobilized. (c) Space-time diagram of the mobilization depth for the same simulation. Measured from the initial flat bed surface at $t = 0$, this depth is locally defined as the maximum depth at which sediment transport has occurred. (d) Evolution of the amplitude of bed forms with respect to time. The two dashed lines in Figures 6c and 6d isolate the same time period. Note that the increase in dune size is synchronous with a deeper mobilization depth.

so-called throughpassing dune. Basically, the initial phase of the collision is the same as for the coalescence into an upstream dominant bed features (see point 2 above). However, when the upstream dune becomes higher, the bed shear stress in the trough and the stoss slope of the downstream dune remain sufficiently high to sustain erosion. Thus, there is no flattening, and the smaller ejected dune can quickly escape away from the recirculation zone of the impacting dune. As they collide with the next bed features downstream, throughpassing dunes produce distinctive diagonal strips cutting through space-time diagrams of dune elevation (Figure 5d).

During the development of bed forms, all dune interactions may be classified into these three types of collisions. However, higher levels of complexity may be reached when different types of collisions occur simultaneously on adjacent dunes or on both sides of the same dunes. In addition, as a consequence of changes in dune velocity, an individual collision is likely to produce a cascade of events. This is typically the case for throughpassing dunes but also very common for coalescence in upstream dominant bed forms.

A major innovation of our 3-D dune model is that it allows for identification and visualization of sedimentary structures at different stages of the evolution of dune fields. Then, sedimentary structures associated with pattern coarsening can be numerically investigated and compared to recognized styles of stratigraphy [*Kocurek*, 1991]. In all simulations, coalescence in upstream dominant bed forms is more frequent than coalescence in downstream dominant bed forms. As a result, sedimentary records of dune fields during the coarsening phase exhibit horizontal stratifications in addition to the classical strata associated with the angle of repose (Figures 6a and 6b). As the sediment is deposited by the impacted dune and recovered during the passage of the impacting dune, the horizontal strata are preserved until the passage of a dune trough with a similar size. Where there is a cascade of merging events, this type of sedimentary structures may persist. Interestingly, these bounding surfaces resemble the sedimentary structures produced by climbing dunes in zones where net deposition is occurring [*Rubin and Hunter*, 1982]. This is not the case in our simulations in which the total amount of sediment is constant. Then, we show that cross-stratified beds may be transient sedimentary

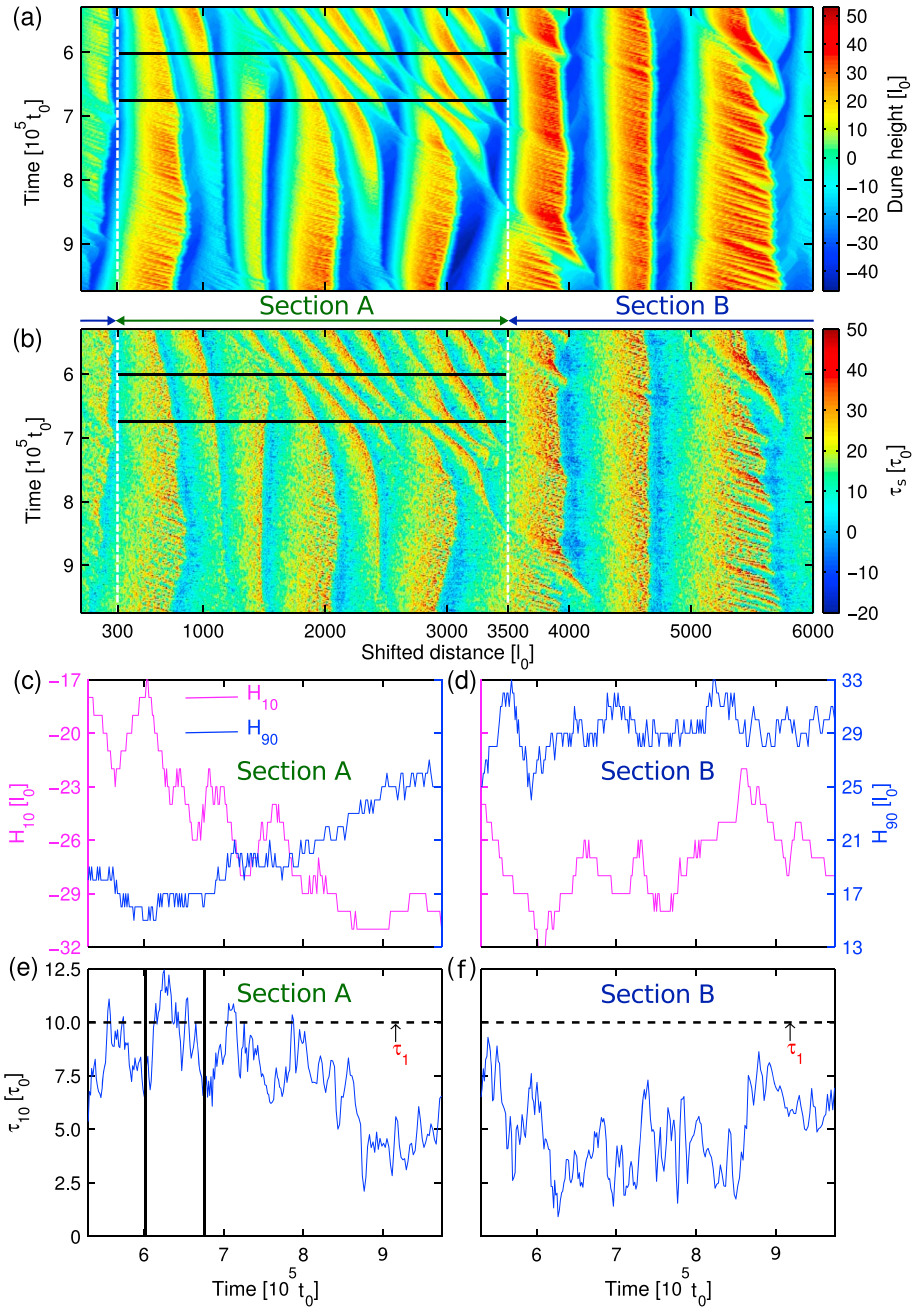

Figure 7. Evolution of topography and bed shear stress during the development of bed forms. (a) Portion of the space-time diagram shown in Figure 3b with a dune topography shifted according to the average dune speed in section B. White dashed lines limit section A, a portion of the space-time diagram where a cascade of merging events occurs. (b) Space-time diagram of the bed shear stress. Note the presence of flow recirculation on the lee sides of dunes (i.e., $\tau_s < 0$). (c) Evolution of H_{10} and H_{90}, the 10th and the 90th percentiles of the height distribution in section A. (d) The same in section B. (e) Evolution of τ_{10}, the 10th percentile of the bed shear stress distribution in section A. (f) The same in section B. The black lines in Figures 7a and 7d limit the same time period. τ_1 is the threshold basal shear stress for motion inception (equation (2)). Note that the cascade of merging events is triggered for $\tau_{10} > \tau_1$. For smaller τ_{10} value, no merging events are observed.

features during dune pattern coarsening. Obviously, in this case, they are only preserved during a local increase in dune size.

Starting from small-amplitude bed forms and given our specific boundary conditions (i.e., no supply of sand from upwind), the average dune size in the model can only increase by mobilizing sediment resources at

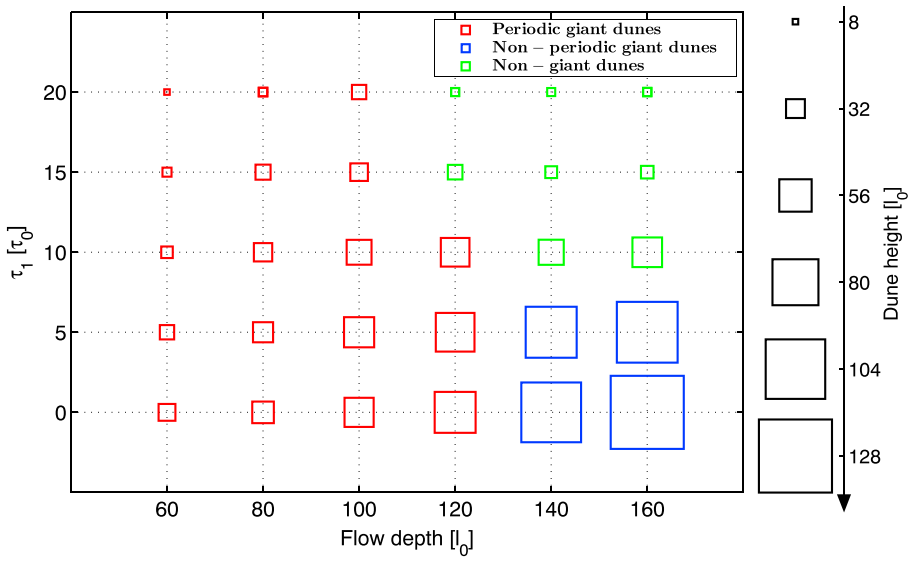

Figure 8. Characterization of the steady state transverse dune fields with respect to flow depth ($F/l_0 = \{60, 80, 100, 120, 140, 160\}$) and flow strength (negatively correlated to $\tau_1/\tau_0 = \{0, 5, 10, 15, 20\}$, the threshold shear stress for motion inception). Within this parameter space, three different classes of steady state dune fields are observed: periodic giant dunes, nonperiodic giant dunes, and nongiant dunes. The characteristic dimension of nongiant dunes is controlled by flow strength rather than by flow depth. Periodic giant dunes form a train of similar bed forms with constant crest-to-crest distance, height, and speed (see Figure 3a). Nonperiodic giant dunes are systematically destabilized by superimposed bed forms and show no periodicity despite a maximum dune size related to flow depth (see Figures 3b–3e). As shown in Figures 3f and 3g, fast Fourier transforms are used to distinguish between periodic and nonperiodic bed forms.

deeper depth (Figures 6c and 6d). Thus, the apparent scouring of the interdune area is a necessary condition for an increase in amplitude of regular transverse dunes. If such a scouring process is enhanced by cascades of merging events upstream and the corresponding decrease of dune velocity, the bed shear stress in the troughs must also be sufficiently high to sustain erosion. Figure 7 shows that collision and merging are likely to be controlled by the magnitude of the bed shear stress in the interdune area. Indeed, a cascade of merging events is triggered in section A (Figures 7a–7c and 7e) where the bed shear stress in the trough is significantly higher than its threshold for motion inception (i.e., the τ_1 value in equation (2)). In section B (Figures 7a, 7b, 7d, and 7f), where the bed shear stress in the trough is already lower than this threshold value, there is no significant change in dune morphology and dynamics. Ultimately, the bed shear stress in the troughs reaches everywhere the same stationary value ($\tau_s < \tau_1$), which corresponds to an equilibrium state for the steady propagation of a train of dunes. This marks the end of the coarsening phase.

4. Effect of Flow Depth and Flow Strength on the Steady State of Transverse Dunes

In all the simulations, dune pattern coarsening stops after some time and the dune fields always reach a steady state. This steady state can be investigated independently of cumulative transport to estimate the characteristic amplitude and wavelength of transverse dune fields. Within the parameter space of this numerical experiment, three classes of steady state transverse dune fields are observed:

1. For high flow speeds (i.e., small τ_1 values) and low flow depths, dunes with similar height and shape propagate at a constant speed. They are defined as periodic giant dunes because their size and wavelength are increasing with flow depth (red squares in Figure 8).
2. At high flow depth and high flow speed, secondary bed forms initiate and develop by merging on the stoss slope of primary dune features. When these primary dunes increase in size (i.e., larger flow depth), incipient dunes can also grow to a larger size by the time they reach the brink of their host dunes. Then, as they approach the dune summit, secondary dunes may become the dominant bed form and eject a smaller dune downstream. Such a mechanism of upstream dominant superimposed bed form is an important dune height saturation mechanism, which does not require collision. However, ejected dunes may also in turn affect the stability of the downstream train of dunes (i.e., see throughpassing bed forms in section 3.2 and

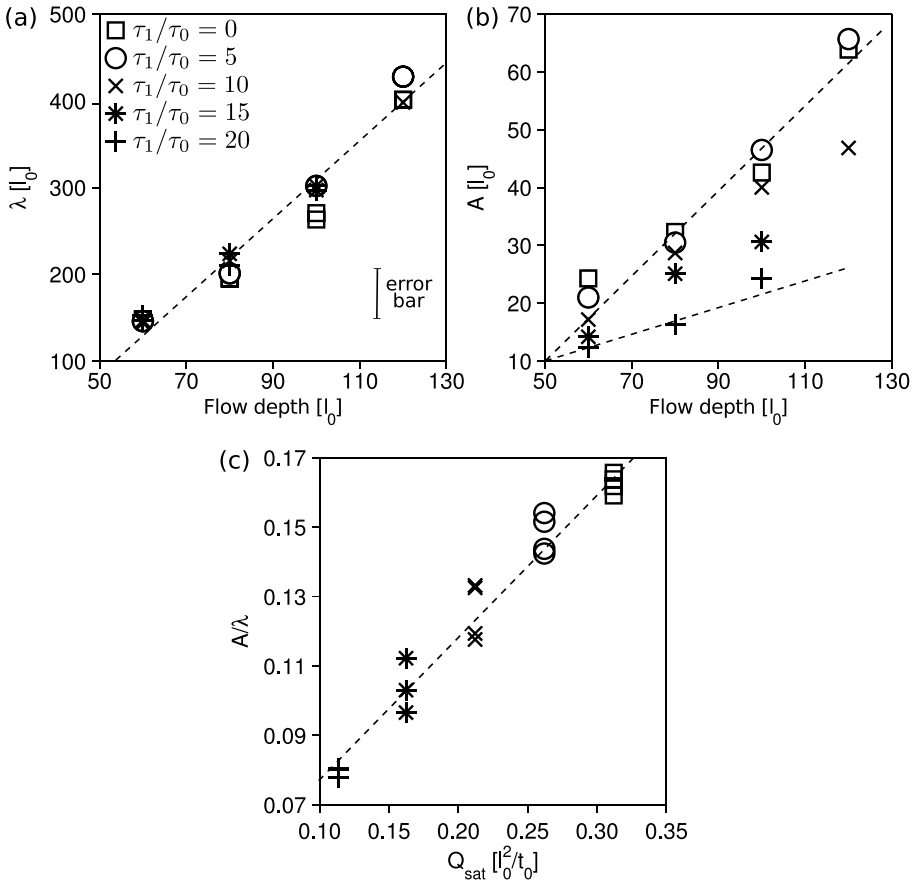

Figure 9. Amplitude, wavelength, and aspect ratio of steady state transverse dune fields with respect to flow depth and strength. (a) Mean crest-to-crest distance with respect to flow depth. The dashed line shows a linear fit to the data. (b) Mean dune height with respect to flow depth. Dashed lines show the linear fits for $\tau_1/\tau_0 = 0$ and $\tau_1/\tau_0 = 20$. (c) Dune aspect ratio with respect to the saturated flux over a flat sand bed. To estimate this flux, we use the analytical expression suggested by *Gao et al.* [2014]: $Q_{sat} = (\Lambda_t/\Lambda_d)\int_0^\infty f(\tau_s)\Lambda_e(\tau_s)\mathrm{d}\tau_s$, where $f(\tau_s)$ is the distribution of the bed shear stress over a flat sand bed. Dashed line shows a linear fit to the data.

Figure 5). Thus, at high flow depth and high flow strength, crest-to-crest distances and dune heights are permanently changing over time and space. Nevertheless, the mean amplitude and wavelength still have upper limits that are an increasing function of flow depth. Then, this quasi-stationary steady state is defined as nonperiodic giant dunes (blue squares in Figure 8).

3. At lower flow strength (i.e., higher τ_1 values), another transition occurs for an increasing flow depth. In this case, the saturation mechanism does not result from the top boundary conditions but is related to the threshold shear stress for motion inception. Indeed, dune growth is limited by the magnitude of the bed shear stress in the interdune areas (Figure 7). As a result, flow strength controls both the height and the wavelength of the regular dune pattern. These dunes are defined as nongiant dunes (green squares in Figure 8).

The selected wavelength of the steady state giant dune fields is directly related to flow depth (Figure 9a) and shows no dependence on flow strength. On the opposite, as discussed above, dune height depends on both flow depth and strength (Figure 9b). Finally, the dune aspect ratio seems linearly related to the amplitude of the saturated sand flux (Figure 9c). Such a dependence indicates that the transverse dune shape is not constant and adapts to flow strength. As for barchan dunes in the model [*Zhang et al.*, 2010] and in laboratory experiments [*Groh et al.*, 2008], the aspect ratio of transverse dunes increases with flow strength. This is a combination of two factors: higher shear stress can sustain steeper slopes and dunes flatten if, in their lower parts, the bed shear stress is below its threshold value for motion inception.

To investigate the response of steady state transverse dune fields to changes in flow conditions, Figure 10 shows how the amplitude, the wavelength, and the bed shear stress in the dune trough areas adapt to a

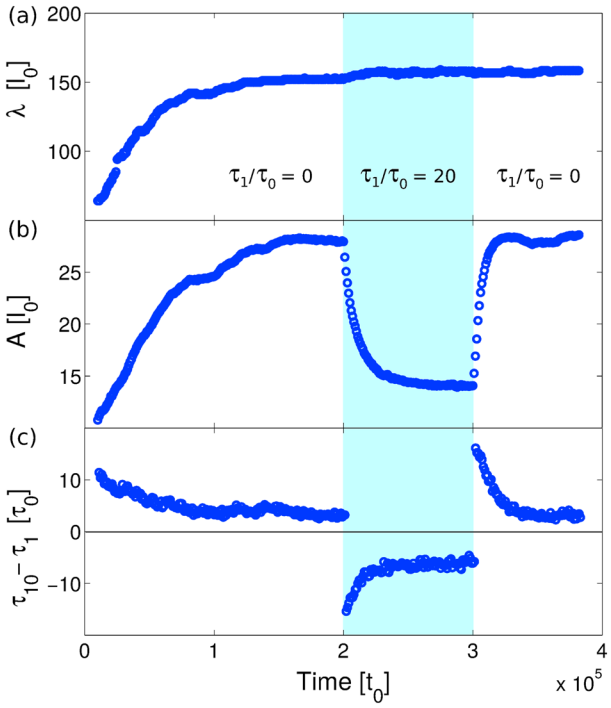

Figure 10. Response of a steady state dune field to a transient change in flow speed keeping a constant flow depth $F/l_0 = 60$: (a) wavelength, (b) amplitude, and (c) difference between the basal shear stress in troughs (τ_{10}, see Figure 7) and the threshold for motion inception (τ_1; see equation (2)). $\tau_1/\tau_0 = 0$, except when $2 \times 10^5 < t/t_0 < 3 \times 10^5$ where $\tau_1/\tau_0 = 20$. For visibility, note that the dependency of the t_0 value on the τ_1 values is not taken into account (see *Narteau et al.* [2009] and *Zhang et al.* [2014, Table 2]). Basically, it would have expanded the timescale when $2 \times 10^5 < t/t_0 < 3 \times 10^5$.

transient decrease in flow speed. By keeping the same flow depth, the characteristic wavelength is not affected by the changes in flow speed (Figure 10a). Following the abrupt reduction in flow speed, the bed shear stress in dune trough areas falls under the threshold for motion inception (Figure 10c at $t/t_0 = 2 \times 10^5$), dunes flatten, dune height is decreasing (Figure 10b), and the entire dune field reaches a new steady state with a smaller dune aspect ratio. When the flow speed is reset to the original value (Figure 10c at $t/t_0 = 3 \times 10^5$), the dune field returns to its previous steady state through the erosion of the troughs where the bed shear stress reaches values larger than the threshold for motion inception. This simulation is a first step in the process of understanding the effect of natural wind regimes on steady state transverse dune fields, a subject which is not in the scope of the present study.

5. Discussion

In this numerical investigation, we use a cellular automaton approach devoted to the modeling of dunes shaped by bed load transport processes. As it neglects the influence of suspension on the overall transport, this model can only explore a limited range of flow speeds for which the bed load is the dominant transport mode. Thus, we study the limit of low flow velocities, a limit relevant for most aeolian dune fields. For subaqueous dunes, all the results may be valid only for systems in which a significant fraction of sediment moving over the crests is trapped in the lee faces [*Mohrig and Smith*, 1996].

The aim of this study is to explore the dynamics of pattern coarsening and the steady states of transverse dune fields in depth-limited flow. Despite the fact that a capping layer has yet to be demonstrated conclusively in aeolian environments, we now use examples from terrestrial sand seas to translate the numerical results to field observations (Figures 11–13). Ultimately, the aeolian case is not the sole focus, and keeping in mind that our model may be rescaled to various physical environments [*Narteau et al.*, 2009], we consider that our numerical results could also be exploited to characterize subaqueous dunes as well as bed forms on other planetary bodies (e.g., Mars and Titan).

5.1. Dune Pattern Coarsening

We simulate transverse dune fields in narrow flumes to concentrate on 2-D dune-dune interactions during the development of bed forms. The three observed types of dune interacting features are the same as those determined experimentally by *Coleman and Melville* [1996]. As in their subaqueous experiments, most of the merging events are driven by the growth of a (smaller) bed form that collides and absorbs all the sedimentary material of the next (larger) downstream dune. In comparison, there are few merging events during which the slip face of the impacting dune slowly vanishes as it propagates on the stoss slope of the larger dune. This difference in proportion is even more marked when the dune size is increasing. It may be different for crescentic barchan dunes for which the same types of collision and coalescence dynamics have been observed [*Hersen and Douady*, 2005; *Katsuki et al.*, 2005; *Vermeesch*, 2011; *Hugenholtz and Barchyn*, 2012; *Bo and Zheng*, 2013; *Génois et al.*, 2013]. Indeed, the lateral slope of these isolated dunes may significantly increase the transverse

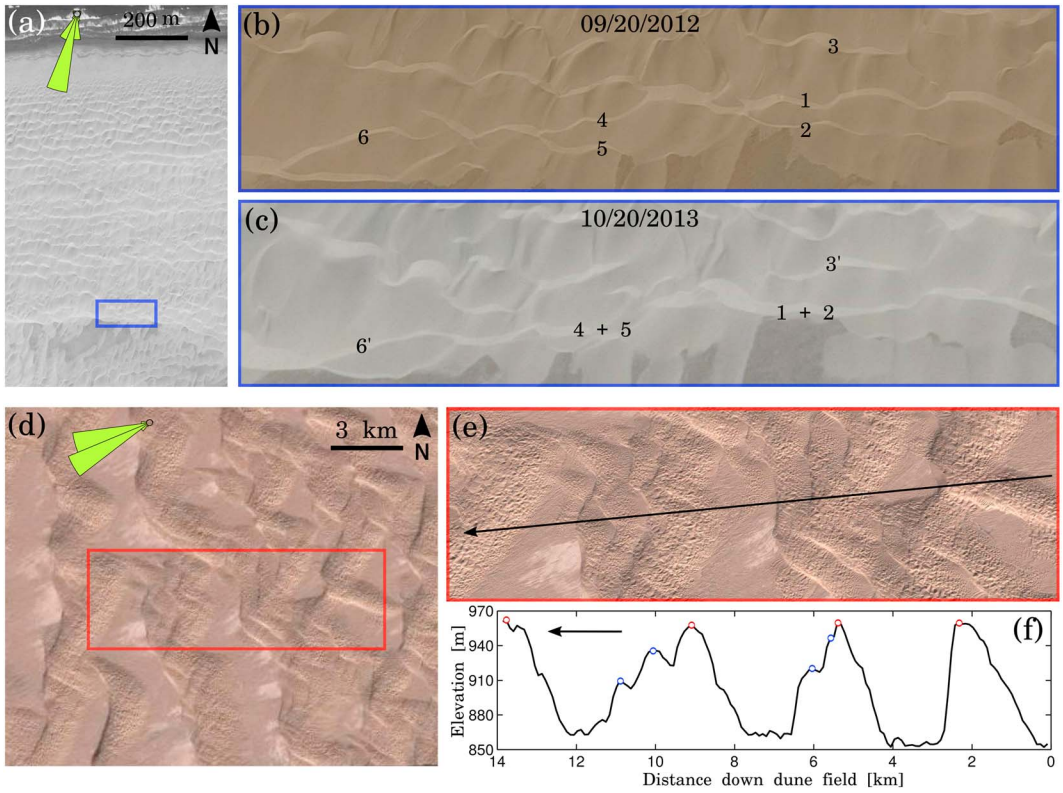

Figure 11. Collision and coalescence into upwind dominant bed forms at two different length scales: (a) Transverse dune field in the Atlantic Sahara desert (Morocco, 28°03′S, 12°13′E). (b and c) The area in the blue box is enlarged for two different times. From Figures 11b to 11c dunes 1 and 2 merge into one dune 1 + 2; dunes 4 and 5 merge into one dune 4 + 5; and dunes 3 and 6 migrate downwind and become dunes 3′ and 6′, respectively. Downwind dunes slowly disappear in their own slip faces as they are recovered by the upwind dunes. (d) Transverse dune field in the East Taklamakan desert (China, 39°24′N, 87°21′E). (e) The area in the red box is enlarged. The arrow shows a transect aligned with the resultant sand transport direction. (f) Topographic profile (Shuttle Radar Topography Mission (SRTM) data with a spatial resolution of 90 m) along this transect line. Red dots show the summit of the upwind dominant bed forms. Blue dots show the summit of the downwind bed forms. They are slowly disappearing in their own slip faces which are abnormally high with respect to their stoss slopes. In Figures 11a and 11d, insets show the local sand flux rose.

component of transport [*Zhang et al.*, 2014] and promotes the slow disappearance of the impacting dune. These lateral fluxes are likely to be much smaller on transverse dunes, and our results indicate that impacting dunes may be resilient to an increase in slope of the longitudinal topographic profiles.

Our classification of 2-D interacting features provides an elementary level of description, which can be used to decompose and analyze the complex dynamics of 3-D bed forms. In particular, this classification can help in understanding how defects and terminations contribute to dune pattern coarsening. For example, *Werner and Kocurek* [1999] propose an analytical model of dune growth in which they introduce a parameter to characterize the crest line loss during the passage of defects through bed forms. Thus, they consider that collision and coalescence occur at the defect tip while collision and ejection occur where the defect is higher [see *Werner and Kocurek*, 1999, Figure 2a]. The sediment being redistributed in the impacted dune, crest line loss is systematically associated with an increase in wavelength. Then, finding the limit in dune height and flow strength for which collisions operate transitions from coalescence to ejection [*Nishimori et al.*, 1998], our classification could be extended to 3-D interacting features to quantify crest line loss in dune fields. In contrast to the model of *Werner and Kocurek* [1999], our simulations have also shown that even in 2-D, the steady state of dune fields may depend on the continuous generation of smaller structures (i.e., defects).

Collision and coalescence into upwind dominant bed forms can be recognized in the field where there is a succession of stoss slopes and slip faces downstream of the summit of the primary dune features. Figure 11 shows examples of coalescence into upwind dominant bed forms at two different length scales. In both cases, the slip faces of the downwind bed forms are abnormally high with respect to their stoss slopes. Within the

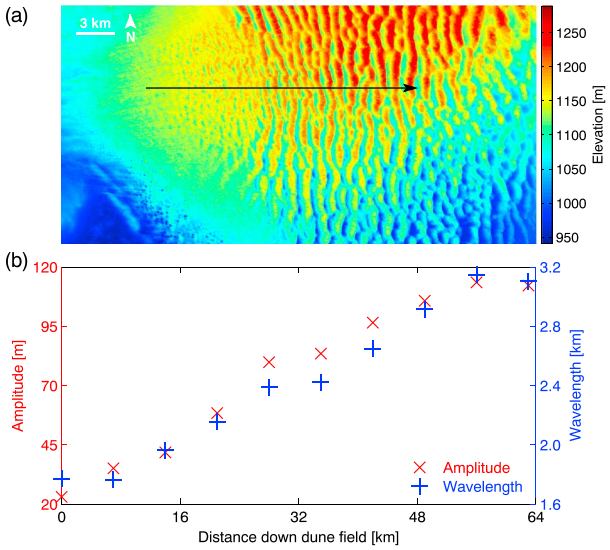

Figure 12. Dune pattern coarsening in the Registan desert (Afghanistan, 30°41′N, 65°40′E). (a) Topographic map of the Registan desert using SRTM digital elevation data with a spatial resolution of 90 m. The sand source is the Helmand river located 50 km to the west of the western boundary of the map. (b) Amplitude and wavelength as a function of the distance along the transect shown in Figure 12a.

shadow zone of the dominant upstream bed form, these stoss slopes systematically flatten as their sediment is continuously redistributed within their own slip faces. Recovered by upstream dunes which evolve in a similar way, it produces a hierarchy of bounding surfaces shown in Figure 6. Thus, we propose that dune pattern coarsening alone may be responsible for the development of a recognized style of stratigraphy [*Rubin and Hunter*, 1982; *Kocurek*, 1991]: dipping at the angle of repose, first-order bounding surfaces are associated with the propagation of individual transverse bed forms through a process that involves reworking their own sediment; almost horizontal, second-order bounding surfaces are associated with collisions and show how upstream dunes continuously absorb the material of the impacted dunes on the top of which they are climbing. These second-order bounding surfaces give the height and the time at which the upstream bed form became the dominant one. On the other hand, coalescence in downstream dominant bed forms leaves no trace in the sedimentary records as it occurs on the stoss slope of the impacted dune, which is systematically remobilized by the wind.

Modern dune fields are likely the result of a long-term evolutionary process, such that individual dunes may have already reached their giant size in most terrestrial deserts. In addition, the development of these dune fields depends strongly on boundary conditions such as wind regime and sediment supply [*Ewing and Kocurek*, 2010; *Eastwood et al.*, 2011]. For this reason, the coarsening phase is difficult to observe with respect to time in a natural aeolian environment without a dedicated experimental setup [*Ping et al.*, 2014]. Alternatively, the development of transverse dunes may be observed in space when they grow in height and propagate from a localized source of sediment subjected to unidirectional winds [*Kocurek and Ewing*, 2005; *Ewing et al.*, 2006]. However, even in this case, an excessive input sediment flux may generate a major transverse dune upwind, which could affect the morphodynamics of the dune fields downwind [*Jerolmack et al.*, 2012]. A rare example of the development of aeolian transverse dune fields without the side effects of the boundary conditions may be found in the Registan desert in Afghanistan (Figure 12). In this arid desert subjected to west winds (Figure 1f), despite the complexity of the superimposed bed forms, the large-scale transverse dune pattern exhibits a constant linear increase in wavelength and amplitude over more than 60 km [*Ewing and Kocurek*, 2010]. Then, it stabilizes to its giant dimensions before being stopped by the central Brahui mountain range. These linear increases of both the crest-to-crest spacing and dune height with respect to distance are in good agreement with the result presented in Figure 4. Indeed, the downwind distance may be converted to time using a distance-time relation that takes into account that the dune speed scales as the inverse of dune height [*Bagnold*, 1941]. Unfortunately, the precision of the digital elevation model and the range of length scale studied do not allow us to distinguish between scaling exponent of 1/2 or 1/3.

5.2. Steady State Transverse Dune Fields

We propose two mechanisms for the interruption of pattern coarsening in transverse dune fields. The first is directly related to the confinement of the flow and leads to the concept of giant dunes, i.e., a characteristic wavelength that scales with the depth of the flow [*Elbelrhiti*, 2005; *Valance*, 2011]. The other one, which has received less attention, is related to the strength of the flow. We show that there is an upper limit in dune size above which a given flow condition is not able to sustain erosion in dune troughs. This is directly associated with the threshold shear stress for bed load transport. Then, we infer that when the stationary dune size is independent of flow depth, the mean basal shear stress in the interdune areas is likely to be close to its

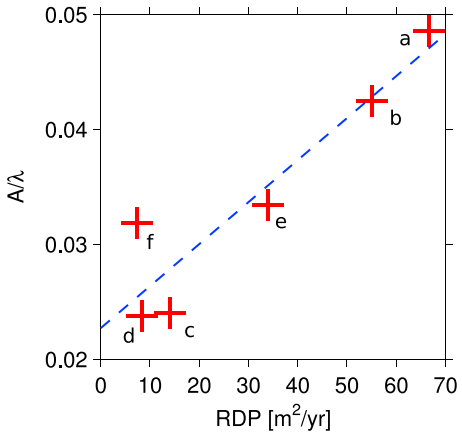

Figure 13. Aspect ratio of transverse dune fields in arid desert on Earth. Amplitude and wavelength are estimated from SRTM data with a spatial resolution of 90 m. The letter refers to labels in Figure 1. See Appendix B for the estimation of the RDP value. The dashed line is the best linear fit.

threshold value for motion inception. Hence, under constant flow conditions, dunes should increase in size with decreasing grain size. Such a relation may be difficult to test in the field because of fluctuating flow conditions and the timescale involved in the development of bed forms, especially in aeolian settings [*Pelletier and Jerolmack*, 2014]. However, following the precursory works of *Fredsoe* [1982] and *van Rijn* [1982], new sets of laboratory experiments exploring different grain sizes and low ranges of flow strength should be able to reproduce such relationships between dune dimension, grain size, and the threshold shear stress value for bed load transport.

When the characteristic length scale of transverse dune fields is controlled by flow depth, we show that the periodicity of giant dunes is affected by the growth of secondary bed forms. Following the linear dune instability on the stoss slopes of large dunes, the coarsening dynamics of superimposed bed forms is the same as for the primary dune features (see section 3.2). Ultimately, as they approach the main ridge of the host dunes, primary and secondary dunes may have the same height and they can directly interact with each other. Then, the underlying host dunes may be destabilized by incipient dunes, especially in the limit of high flow depth (i.e., larger dunes). As during collisions (see section 3.2 and *Vermeesch* [2011, Figure 1] for an example in nature), the newly formed dune may eject downstream what was the dominant bed form before. These ejections will affect the entire train of dunes and may be responsible for the break in periodicity. Alternatively, this systematic formation of secondary dune features may also be described as a continuous source of calving, which increases the defect density in transverse dune fields. For barchan dune fields, it also indicates that calving may also occur in the central part of the dune and not only along horns [*Elbelrhiti*, 2005; *Zhang et al.*, 2010; *Worman et al.*, 2013]. Then, without calling for collisions, it could explain the ejection of smaller dunes in this central area of giant barchan dunes.

In the limit of high flow strength, when the increase in dune size is interrupted by the depth of the flow, we show that the morphology of giant dune fields results from a dynamic equilibrium between dune steepness and bed shear stress. In fact, with no change in sand availability, the dune aspect ratio is the only adjustable quantity for the stability of transverse dune fields. As observed by *Raudkivi* [1976], *Yalin* [1977], and *Groh et al.* [2008] for small bed shear stress (i.e., no suspension), we find that there is an increasing dune aspect ratio for an increasing flow strength: higher flow conditions can sustain transport on steeper slopes and maintain a strong aspect ratio, which is in turn responsible for an increase of the acceleration of the flow over the dune stoss slopes.

The dependence of the wavelength of aeolian giant dunes on flow depth has been proposed and quantified by *Andreotti et al.* [2009]. The presence of such a capping layer deserves to be examined more carefully, but our study is not a test of its existence; it is rather an exploration of the outcomes of capping flow on bed form morphology. Under such boundary condition, our numerical simulations show that the characteristic wavelength of giant transverse dune fields scales as the depth of the flow (Figure 9). Using an independent set of data from the ERA-Interim project, the latest global atmospheric reanalysis produced by the European Centre for Medium-Range Weather Forecasts [*Simmons et al.*, 2007; *Dee et al.*, 2011], we have been able to reproduce the same observations (see Appendix A). In addition, we can complete this work by analyzing the relation between the dune aspect ratio and the strength of the flow using more than 30 years of wind data (see Appendix B) and the digital elevation model of the various dune fields shown in Figure 1. Figure 13 shows that as predicted by our model, there is a linear relation between the RDP value and the dune aspect ratio. Hence, the morphology of the dune (i.e., wavelength and amplitude) could be used to infer not only the depth of the flow but also the mean flow strength in regions where it cannot be directly measured. Dealing with such an inverse problem in the future, difficulties will arise from the variability in wind strength and the long-term history of the climatic conditions that may have contributed to the shape of the largest dunes.

Table 1. Morphological Properties of Transverse Dune Fields Shown in Figure 1 (Wavelength λ and Amplitude A) and Local Flow Properties Derived From the ERA-Interim Data (Resultant Drift Potential RDP, Height of the Atmospheric Boundary Layer H)[a]

Dune Fields	λ (km)	A (m)	RDP (m^2/yr)	H^* (km)	H (km)	T_{dune} (year)
(a)	0.7	34	66.7	0.5	0.6	17.3
(b)	0.4	17	55.1	–	0.8	5.2
(c)	0.5	12	14.1	0.7	0.7	10.2
(d)	3.2	76	8.4	3.1	3.6	687.6
(e)	3.0	100	33.9	3.4	4.0	295.0
(f)	2.2	70	7.4	2.3	3.1	662.2

[a] H^* is the depth of the atmospheric boundary layer measured by *Andreotti et al.* [2009]. For comparison with the duration of 33 years of the ERA-Interim data, $T_{dune} = A^2/\mathrm{RDP}$ is the characteristic renewal time of the transverse dune fields.

The same caveats and limitations apply to the data shown in Figure 13, especially for the largest dunes which have a characteristic renewal time longer than the duration of the wind data (see Table 1 and Figure 1).

6. Conclusion

Using a numerical model for the formation and the development of bed forms, we provide a physical classification of the different types of dune-dune interactions that govern pattern coarsening in transverse dune fields. Thus, we are able to establish relationships between surface morphology and the preserved sedimentary structures at depth. This aspect of the problem has yet to be worked out, but it is already evident that merging in upstream dominant bed forms needs more attention in the future. Concerning the steady state of transverse dune fields, we show that both the depth and the strength of the flow have an effect on the final dune shape by interrupting the coarsening phase. When the strength of the flow is the limiting factor, transverse dune fields should not be considered as giant dunes. In all cases, we also find that the dune aspect ratio could be positively correlated to the strength of the flow. We infer that dune steepness can then be used to estimate flow conditions in various environments.

Appendix A: Depth of the Atmospheric Boundary Layer

The depth H of the atmospheric boundary layer (ABL) is highly variable in time, strongly influenced by seasonal and daily cycles of surface heating and cooling. Here using the ERA-Interim project for over a time period ΔT of 34 years, from 1 January 1979 to 31 December 2012 with a time resolution $\Delta t = 6$ h, we estimate this depth following the procedure proposed by *Andreotti et al.* [2009].

From the 10 m temperature T and surface pressure P, we compute the virtual potential temperature

$$\Theta = T_v \left(\frac{P_0}{P}\right)^{R/C_p}, \tag{A1}$$

where $P_0 = 10^5$ Pa is a reference pressure, $R = 8.31$ J/K the perfect gas constant, $C_p = 29.19$ J/K the air molar heat capacity, and T_v the virtual temperature. According to *Bailey* [2000], the T_v value is defined as

$$\frac{T}{T_v} = 1 - \left(1 - \frac{M_w}{M_d}\right)\frac{e_s}{P}, \tag{A2}$$

where e_s is the saturated vapor pressure [*Goff*, 1957] and $M_w = 0.018$ kg/Mol and $M_d = 0.029$ kg/Mol are the molecular masses of water and dry air, respectively.

The potential temperature Θ serves as a stability criterion for an atmosphere which has a uniform moisture content. Θ is supposed to be constant in the ABL and to increase above in the free atmosphere, which preserves a steady linear profile of slope $\gamma \approx 4$ K/km. Then, using the amplitude $\delta\theta$ of the annual variation of the temperature, the depth H of the atmospheric boundary layer may be defined as $\delta\theta/\gamma$. This is obviously a rough estimate, and relative variations are more important than the absolute values. For all the dune fields shown in Figure 1, Table 1 shows that the H values estimated from the ERA-Interim data agree with the values calculated by *Andreotti et al.* [2009]. See *Garratt* [1994] for other methods of estimation of the depth of

the atmospheric boundary layer and *Seidel et al.* [2010] for a sensitivity analysis; magnitudes of uncertainties associated with methodological choices are several hundred meters.

Appendix B: Sand Flux Estimation

The wind regimes are characterized by the averaged sand flux roses using the 10 m wind data of the ERA-Interim project presented in Appendix A. The shear velocity can be defined as

$$u_* = \frac{u\kappa}{\log(z/z_0)}, \tag{B1}$$

where u is the wind speed at a height of 10 m, z_0 the surface roughness length, and κ the von Kármán constant. Here we take $z_0 = 10^{-3}$ m and $\kappa = 0.4$. The threshold shear velocity value for motion inception can be determined using the formula calibrated by *Iversen and Rasmussen* [1999],

$$u_{*c} = 0.1\sqrt{\frac{\rho_s}{\rho_f} g \mathrm{d}}, \tag{B2}$$

where $g = 9.81$ m/s^{-2} is the gravitational acceleration, ρ_s/ρ_f the grain to fluid density ratio, and d the grain diameter. Here we take $\rho_s = 2.65 \times 10^3$ kg/m^3 and $\rho_f = 1.27$ kg/m^3. The saturated sand flux on a flat erodible bed can be determined using a relationship proposed by *Ungar and Haff* [1987]:

$$Q(u_*) = 25(\rho_f/\rho_s)\sqrt{\mathrm{d}/g}(u_*^2 - u_{*c}^2). \tag{B3}$$

To calculate the RDP/DP value, we take

$$\mathrm{DP} = \sum \|\overrightarrow{Q(u_*)}\| \Delta t/\Delta T \tag{B4}$$

and

$$\mathrm{RDP} = \left\| \sum \Delta t \overrightarrow{Q(u_*)} \right\| / \Delta T. \tag{B5}$$

Table 1 shows the RDP values for the dune fields shown in Figure 1.

Acknowledgments
We thank three anonymous reviewers for their useful comments on a preliminary version of this manuscript. We are grateful to Sylvain Courrech du Pont, Olivier Devauchelle, Philippe Claudin, and Sébastien Rodriguez for their helpful discussions. The data present in this paper are the result of numerical simulations using ReSCAL. The Real-Space Cellular Automaton Laboratory (ReSCAL) is a free software under the GNU general public licence. The source codes can be downloaded from http://www.ipgp.fr/rescal. The natural wind data supporting Figures 1 and 13 are available at the European Centre for Medium-Range Weather Forecasts (ECMWF), available from http://apps.ecmwf.int/datasets/. The altitude data supporting Figures 11–13 are the Shuttle Radar Topography Mission (SRTM) digital elevation data with a spatial resolution of 90 m (available from http://srtm.usgs.gov/). Images in Figures 1 and 11 are courtesy of Google Earth. We acknowledge financial support from the UnivEarthS LabEx program of Sorbonne Paris Cité (ANR-10-LABX-0023 and ANR-11-IDEX-0005-02) and the French National Research Agency (ANR-09-RISK-004/GESTRANS and ANR-12-BS05-001-03/EXO-DUNES).

References

Allen, J. (1963), Asymmetrical ripple marks and the origin of water-laid Cosets of Cross-Strata, *Geol. J.*, *3*(2), 187–236.
Allen, J. R. (1985), *Principles of Physical Sedimentology*, 272 pp., Allen and Unwin, London.
Andreotti, B., P. Claudin, and S. Douady (2002), Selection of dune shapes and velocities: Part 2. A two-dimensional modelling, *Eur. Phys. J. B*, *28*(3), 341–352.
Andreotti, B., A. Fourrière, F. Ould-Kaddour, B. Murray, and P. Claudin (2009), Giant aeolian dune size determined by the average depth of the atmospheric boundary layer, *Nature*, *457*(7233), 1120–1123.
Baddock, M., I. Livingstone, and G. F. Wiggs (2007), The geomorphological significance of airflow patterns in transverse dune interdunes, *Geomorphology*, *87*(4), 322–336.
Bagnold, R. A. (1941), *The Physics of Blown Sand and Desert Dunes*, 265 pp., Chapman and Hall, London.
Bailey, D. T. (2000), Meteorological Monitoring Guidance for Regulatory Modeling Applications, *Rep.*, U.S. Environment Protection Agency.
Bennett, S., and J. Best (1995), Mean flow and turbulence structure over fixed, two-dimensional dunes: Implications for sediment transport and bedform stability, *Sedimentology*, *42*(3), 491–513.
Best, J. (2005), The fluid dynamics of river dunes: A review and some future research directions, *J. Geophys. Res.*, *110*, F04S02, doi:10.1029/2004JF000218.
Bo, T.-L., and X.-J. Zheng (2013), Collision behaviors of barchans in aeolian dune fields, *Environ. Earth Sci.*, *70*(7), 2963–2970.
Brookfield, M. (1977), The origin of bounding surfaces in ancient aeolian sandstones, *Sedimentology*, *24*(3), 303–332.
Charru, F., B. Andreotti, and P. Claudin (2013), Sand ripples and dunes, *Annu. Rev. Fluid Mech.*, *45*, 469–493.
Chopard, B., and M. Droz (1998), *Cellular Automata Modeling of Physical Systems*, vol. 122, Cambridge Univ. Press, Cambridge.
Claudin, P., and B. Andreotti (2006), A scaling law for aeolian dunes on Mars, Venus, Earth, and for subaqueous ripples, *Earth Planet. Sci. Lett.*, *252*(1), 30–44.
Coleman, S., and B. Melville (1994), Bed-form development, *J. Hydraul. Eng.*, *120*(5), 544–560.
Coleman, S., and B. Melville (1996), Initiation of bed forms on a flat sand bed, *J. Hydraul. Eng.*, *122*(6), 301–310.
Coleman, S., T. Nakato, and R. Ettema (1996), Wave generation and development on a sandy river bed, in *Issues and Directions in Hydraulics, Proc., of Iowa Hydraulics Colloquium*, Balkema, Rotterdam, Netherlands.
Courrech du Pont, S. (2015), Dune morphodynamics, *C. R. Phys.*, *16*(1), 118–138, doi:10.1016/j.crhy.2015.02.002.
Courrech du Pont, S., C. Narteau, and X. Gao (2014), Two modes for dune orientation, *Geology*, *42*(9), 743–746.
Dee, D., et al. (2011), The ERA-Interim reanalysis: Configuration and performance of the data assimilation system, *Q. J. R. Meteorol. Soc.*, *137*(656), 553–597.
Dong, Z., G. Qian, W. Luo, and H. Wang (2007), A wind tunnel simulation of the effects of stoss slope on the lee airflow pattern over a two-dimensional transverse dune, *J. Geophys. Res.*, *112*, F03019, doi:10.1029/2006JF000686.

Dong, Z., G. Qian, W. Luo, Z. Zhang, S. Xiao, and A. Zhao (2009), Geomorphological hierarchies for complex mega-barchan dunes in dunes and their implications for mega-dune evolution in the Badain Jaran Desert, *Geomorphology*, *106*(3–4), 180–185.
Eastwood, E., J. Nield, A. Baas, and G. Kocurek (2011), Modelling controls on aeolian dune-field pattern evolution, *Sedimentology*, *58*(6), 1391–1406.
Elbelrhiti, H. (2005), Morphodynamique des barkhanes: Étude des dunes du Sud-Ouest Marocain, PhD thesis, 154 pp., Univ. Paris Diderot, Paris, France.
Elbelrhiti, H., P. Claudin, and B. Andreotti (2005), Field evidence for surface-wave-induced instability of sand dunes, *Nature*, *437*(7059), 720–723.
Endo, N., T. Sunamura, and H. Takimoto (2005), Barchan ripples under unidirectional water flows in the laboratory: Formation and planar morphology, *Earth Surf. Processes Landforms*, *30*(13), 1675–1682.
Ewing, R., and G. Kocurek (2010), Aeolian dune-field pattern boundary conditions, *Geomorphology*, *114*(3), 175–187.
Ewing, R. C., G. Kocurek, and L. W. Lake (2006), Pattern analysis of dune-field parameters, *Earth Surf. Processes Landforms*, *31*(9), 1176–1191.
Fischer, S., M. E. Cates, and K. Kroy (2008), Dynamic scaling of desert dunes, *Phys. Rev. E*, *77*, 031302, doi:10.1103/PhysRevE.77.031302.
Flemming, B. (2000), The role of grain size, water depth and flow velocity as scaling factors controlling the size of subaqueous dunes, in *Procedures of Marine Sandwave Dynamics*, edited by A. Trentesaux and T. Garlan, pp. 23–24, Univ. of Lille 1, Lille, France.
Fredsoe, J. (1982), Shape and dimensions of stationary dunes in rivers, *J. Hydraul. Div.*, *108*(8), 932–947.
Gao, X., D. Zhang, O. Rozier, and C. Narteau (2014), Transport capacity and saturation mechanism in a real-space cellular automaton dune model, *Adv. Geosci.*, *37*, 47–55, doi:10.5194/adgeo-37-47-2014.
Garratt, J. R. (1994), *The Atmospheric Boundary Layer*, 319 pp., Cambridge Univ. Press, Cambridge.
Génois, M., S. Courrech du Pont, P. Hersen, and G. Grégoire (2013), An agent-based model of dune interactions produces the emergence of patterns in deserts, *Geophys. Res. Lett.*, *40*, 3909–3914, doi:10.1002/grl.50757.
Goff, J. A. (1957), Saturation pressure of water on the new kelvin temperature scale, *Trans. Am. Soc. Heating Vent. Eng.*, *63*, 347–353.
Groh, C., A. Wierschem, N. Aksel, I. Rehberg, and C. A. Kruelle (2008), Barchan dunes in two dimensions: Experimental tests for minimal models, *Phys. Rev. E*, *78*, 021304, doi:10.1103/PhysRevE.78.021304.
Hersen, P., and S. Douady (2005), Collision of barchan dunes as a mechanism of size regulation, *Geophys. Res. Lett.*, *32*, L21403, doi:10.1029/2005GL024179.
Hersen, P., S. Douady, and B. Andreotti (2002), Relevant length scale of barchan dunes, *Phys. Rev. Lett.*, *89*, 264301, doi:10.1103/PhysRevLett.89.264301.
Hugenholtz, C. H., and T. E. Barchyn (2012), Real barchan dune collisions and ejections, *Geophys. Res. Lett.*, *39*, L02306, doi:10.1029/2011GL050299.
Iversen, J. D., and K. R. Rasmussen (1999), The effect of wind speed and bed slope on sand transport, *Sedimentology*, *46*(4), 723–731.
Jackson, P., and J. Hunt (1975), Turbulent wind flow over a low hill, *Q. J. R. Meteorol. Soc.*, *101*(430), 929–955.
Jackson, R. G. (1976), Sedimentological and fluid-dynamic implications of the turbulent bursting phenomenon in geophysical flows, *J. Fluid Mech.*, *77*(03), 531–560.
Jerolmack, D. J., and D. Mohrig (2005), A unified model for subaqueous bed form dynamics, *Water Resour. Res.*, *41*, W12421, doi:10.1029/2005WR004329.
Jerolmack, D. J., R. C. Ewing, F. Falcini, R. L. Martin, C. Masteller, C. Phillips, M. D. Reitz, and I. Buynevich (2012), Internal boundary layer model for the evolution of desert dune fields, *Nat. Geosci.*, *5*(3), 206–209.
Katsuki, A., H. Nishimori, N. Endo, and K. Taniguchi (2005), Collision dynamics of two barchan dunes simulated using a simple model, *J. Phys. Soc. Jpn.*, *74*(2), 538–541.
Kocurek, G. (1991), Interpretation of ancient eolian sand dunes, *Annu. Rev. Earth Planet. Sci.*, *19*, 43–75.
Kocurek, G., and R. Ewing (2005), Aeolian dune field self-organization—Implications for the formation of simple versus complex dune-field patterns, *Geomorphology*, *72*(1), 94–105.
Kocurek, G., R. Ewing, and D. Mohrig (2010), How do bedform patterns arise? New views on the role of bedform interactions within a set of boundary conditions, *Earth Surf. Processes Landforms*, *35*(1), 51–63.
Kroy, K., G. Sauermann, and H. J. Herrmann (2002a), Minimal model for sand dunes, *Phys. Rev. Lett.*, *88*, 054301, doi:10.1103/PhysRevLett.88.054301.
Kroy, K., G. Sauermann, and H. Herrmann (2002b), Minimal model for aeolian sand dunes, *Phys. Rev. E*, *66*, 031302, doi:10.1103/PhysRevE.66.031302.
Mohrig, D., and J. D. Smith (1996), Predicting the migration rates of subaqueous dunes, *Water Resour. Res.*, *32*, 3207–3217, doi:10.1029/96WR01129.
Momiji, H., et al. (2000), Simulation of the effect of wind speedup in the formation of transverse dune fields, *Earth Surf. Processes Landforms*, *25*(8), 905–918.
Narteau, C., J. Le Mouël, J. Poirier, E. Sepúlveda, and M. Shnirman (2001), On a small-scale roughness of the core–mantle boundary, *Earth Planet. Sci. Lett.*, *191*(1), 49–60.
Narteau, C., D. Zhang, O. Rozier, and P. Claudin (2009), Setting the length and time scales of a cellular automaton dune model from the analysis of superimposed bed forms, *J. Geophys. Res.*, *114*, F03006, doi:10.1029/2008JF001127.
Nishimori, H., and N. Ouchi (1993), Formation of ripple patterns and dunes by wind-blown sand, *Phys. Rev. Lett.*, *71*, 197–200, doi:10.1103/PhysRevLett.71.197.
Nishimori, H., M. Yamasaki, and K. Andersen (1998), A simple model for the various pattern dynamics of dunes, *Int. J. Mod. Phys. B*, *12*(03), 257–272.
Parsons, D., I. Walker, and G. Wiggs (2004), Numerical modelling of flow structures over idealized transverse aeolian dunes of varying geometry, *Geomorphology*, *59*(1), 149–164.
Parteli, E., V. Schwämmle, H. Herrmann, L. Monteiro, and L. Maia (2006), Profile measurement and simulation of a transverse dune field in the Lençóis Maranhenses, *Geomorphology*, *81*(1), 29–42.
Pelletier, J. D. (2009), Controls on the height and spacing of eolian ripples and transverse dunes: A numerical modeling investigation, *Geomorphology*, *105*(3), 322–333.
Pelletier, J. D., and D. J. Jerolmack (2014), Multiscale bed form interactions and their implications for the abruptness and stability of the downwind dune field margin at White Sands, New Mexico, USA, *J. Geophys. Res. Earth Surf.*, *119*, 2396–2411, doi:10.1002/2014JF003210.
Ping, L., C. Narteau, Z. Dong, Z. Zhang, and S. Courrech du Pont (2014), Emergence of oblique dunes in a landscape-scale experiment, *Nat. Geosci.*, *7*(2), 99–103.
Politi, P., and C. Misbah (2004), When does coarsening occur in the dynamics of one-dimensional fronts?, *Phys. Rev. Lett.*, *92*, 090601, doi:10.1103/PhysRevLett.92.090601.

Qian, G., Z. Dong, W. Luo, and H. Wang (2009), Variations of horizontal and vertical velocities over two-dimensional transverse dunes: A wind tunnel simulation of the effect of windward slope, *J. Arid Environ.*, *73*(12), 1109–1116.
Raudkivi, A. J. (1976), *Loose Boundary Hydraulics*, 397 pp., Pergamon Press, Oxford.
Raudkivi, A. J. (1997), Ripples on stream bed, *J. Hydraul. Eng.*, *123*(1), 58–64.
Reffet, E., S. Courrech du Pont, P. Hersen, and S. Douady (2010), Formation and stability of transverse and longitudinal sand dunes, *Geology*, *38*(6), 491–494.
Richards, K. J. (1980), The formation of ripples and dunes on an erodible bed, *J. Fluid Mech.*, *99*(03), 597–618.
Rozier, O., and C. Narteau (2014), A real-space cellular automaton laboratory, *Earth Surf. Processes Landforms*, *39*(1), 98–109.
Rubin, D. M., and R. E. Hunter (1982), Bedform climbing in theory and nature, *Sedimentology*, *29*(1), 121–138.
Sauermann, G., K. Kroy, and H. J. Herrmann (2001), Continuum saltation model for sand dunes, *Phys. Rev. E*, *64*, 031305, doi:10.1103/PhysRevE.64.031305.
Schwämmle, V., and H. Herrmann (2004), Modelling transverse dunes, *Earth Surf. Processes Landforms*, *29*(6), 769–784.
Seidel, D. J., C. O. Ao, and K. Li (2010), Estimating climatological planetary boundary layer heights from radiosonde observations: Comparison of methods and uncertainty analysis, *J. Geophys. Res.*, *115*, D16113, doi:10.1029/2009JD013680.
Simmons, A., S. Uppala, D. Dee, and S. Kobayashi (2007), ERA-interim: New ECMWF reanalysis products from 1989 onwards, *ECMWF Newsletter*, *110*(110), 25–35.
Southard, J. B. (1991), Experimental determination of bed-form stability, *Annu. Rev. Earth Planet. Sci.*, *19*, 423–455.
Stull, R. B. (1988), *An Introduction to Boundary Layer Meteorology*, 673 pp., Kluwer Acad., Dordrecht, Netherlands.
Ungar, J., and P. Haff (1987), Steady state saltation in air, *Sedimentology*, *34*(2), 289–299.
Unsworth, C., D. Parsons, and S. McLelland (2013), On the scaling of dune bedforms: Flow depth and shear stress. Presented at: International Conference on Fluvial Sedimentology 10, Leeds, U. K., 14–19 July.
Valance, A. (2011), Nonlinear sand bedform dynamics in a viscous flow, *Phys. Rev. E*, *83*, 036304, doi:10.1103/PhysRevE.83.036304.
van Rijn, L. C. (1982), Equivalent roughness of alluvial bed, *J. Hydraul. Eng.*, *108*(10), 1215–1218.
Venditti, J. G., M. Church, and S. J. Bennett (2005), Morphodynamics of small-scale superimposed sand waves over migrating dune bed forms, *Water Resour. Res.*, *41*, W10423, doi:10.1029/2004WR003461.
Vermeesch, P. (2011), Solitary wave behavior in sand dunes observed from space, *Geophys. Res. Lett.*, *38*, L22402, doi:10.1029/2011GL049610.
Walker, I. J., and W. G. Nickling (2003), Simulation and measurement of surface shear stress over isolated and closely spaced transverse dunes in a wind tunnel, *Earth Surf. Processes Landforms*, *28*(10), 1111–1124.
Wasson, R., and R. Hyde (1983), Factors determining desert dune types, *Nature*, *304*, 337–339.
Werner, B. (1995), Eolian dunes: Computer simulations and attractor interpretation, *Geology*, *23*(12), 1107–1110.
Werner, B., and G. Kocurek (1999), Bedform spacing from defect dynamics, *Geology*, *27*(8), 727–730.
Wiggs, G. F., I. Livingstone, and A. Warren (1996), The role of streamline curvature in sand dune dynamics: Evidence from field and wind tunnel measurements, *Geomorphology*, *17*(1), 29–46.
Worman, S. L., A. B. Murray, R. Littlewood, B. Andreotti, and P. Claudin (2013), Modeling emergent large-scale structures of barchan dune fields, *Geology*, *41*(10), 1059–1062.
Yalin, M. S. (1964), Geometrical properties of sand waves, *J. Hydraul. Div. Am. Soc. Civ. Eng*, *90*(5), 105–119.
Yalin, M. S. (1977), *Mechanics of Sediment Transport*, 298 pp., Pergamon press, New York.
Zhang, D., C. Narteau, and O. Rozier (2010), Morphodynamics of barchan and transverse dunes using a cellular automaton model, *J. Geophys. Res.*, *115*, F03041, doi:10.1029/2009JF001620.
Zhang, D., C. Narteau, O. Rozier, and S. Courrech du Pont (2012), Morphology and dynamics of star dunes from numerical modelling, *Nat. Geosci.*, *5*(7), 463–467.
Zhang, D., X. Yang, O. Rozier, and C. Narteau (2014), Mean sediment residence time in barchan dunes, *J. Geophys. Res. Earth Surf.*, *119*, 451–463, doi:10.1002/2013JF002833.